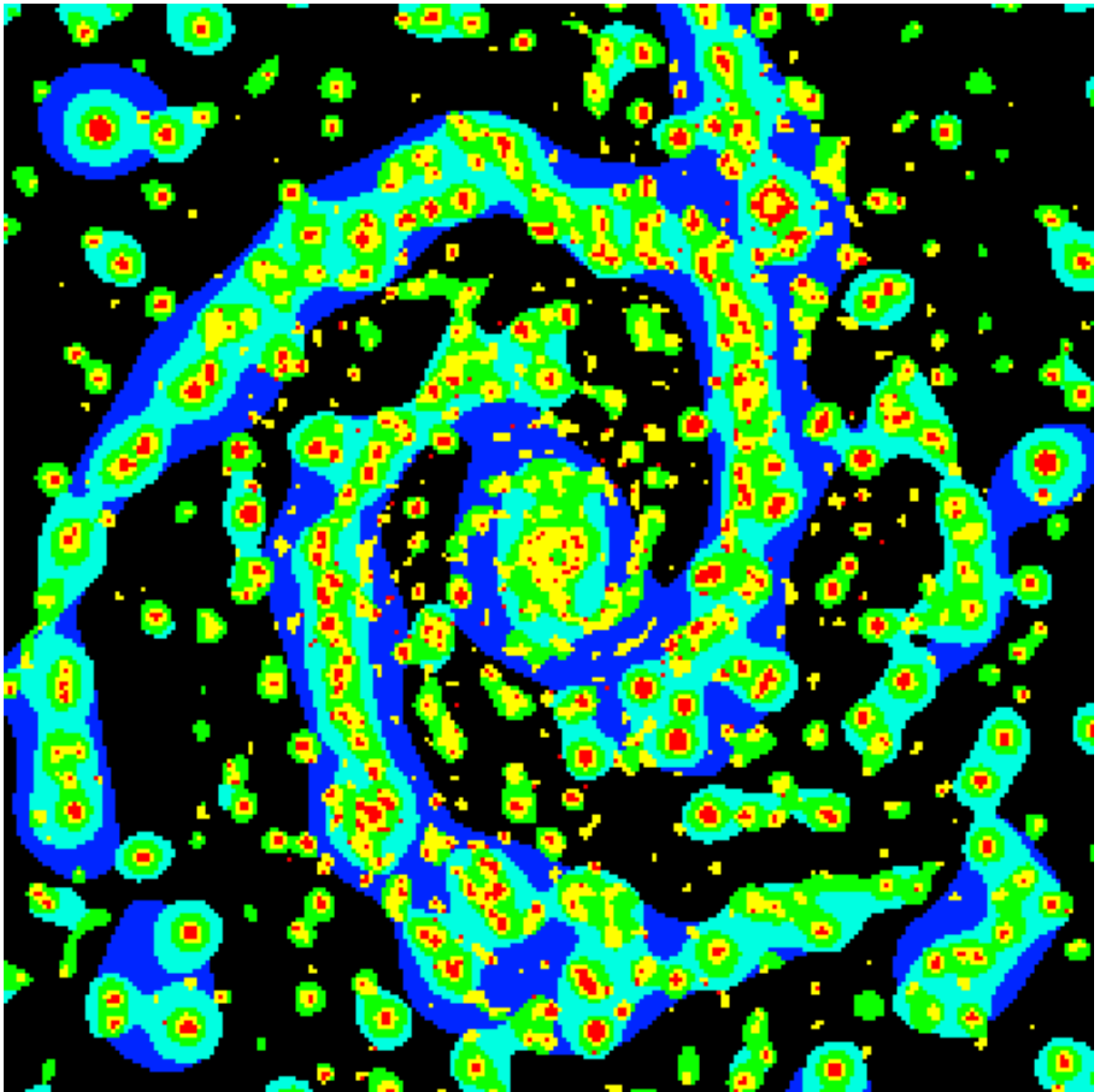# Multiresolution and its Applications: an Overview

J.-L. STARCK

DAPNIA/SEI-SAP, CEA/Saclay,
F-91191 Gif sur Yvette Cedex, France
jstarck@cea.fr

Contents

1 Introduction

Multiresolution techniques have been developed during recent years, and furnish a powerful representation of the data. By means of such techniques an image can be decomposed into a set of images (or scales), each scale containing only structures of a given size. This data representation, associated with noise modeling, have been applied to diverse applications:

- Deconvolution: this consists of subtracting out the instrumental effects on the data. Such effects can be seen as loss in resolution. The noise makes this task impossible (there is no unique solution) unless some constraints are added. Our work shows that these constraints can be expressed in the wavelet space, which allows us to take the noise statistics into account in a much improved way.

- Spectral analysis. Again, wavelets lead to a new approach for data analysis, and absorption band detection with a low signal-to-noise ratio is one example, as well as extraction of parameters such as the medium optical depth.

- X-ray image analysis (e.g. from the ROSAT satellite) by the wavelet transform. Sources can be detected in an automatic way, and images can be restored, allowing us to carry out galaxy cluster morphological analysis.

- Image compression: a method based on multiresolution has been created. This allows a high compression ratio, by keeping a visual, astrometric (location-related), and photometric (intensity-related) quality for the objects contained in the image. This method allows us also to decompress the image at a lower resolution, which could be an advantage for the transfer of images from an image database. Indeed, a user can quickly visualize an image at low resolution, and if it is of sufficient interest, he can continue the transfer to the following levels of resolution (this is known as progressive transmission). An extensive study carried out at Strasbourg Data Center (CDS) demonstrates that a ratio of 260 can be obtained with an acceptable quality for ESO Schmidt data, digitized with the MAMA machine. The JPEG norm allows only a compression ratio of 40 for the same quality.

- ISOCAM (a camera on board ISO, Infrared Satellite Observatory) faint source detection. Cosmic ray impact suppression in ISOCAM data.

- Image registration in Earth observation.

The good quality of the results furnished by methods using multiresolution analysis is due to the fact that multiresolution analysis allows us to better understand how the information is distributed in an image, and how the signal can be separated from the noise.

The software developed includes almost all applications presented in the book *Image and Data Analysis: The Multiscale Approach* [34], and is integrated into a system produced by the CEA and Nice Observatory. This software contains at the current time around 100,000 lines of code (C++), a set (10,000 lines) of IDL (Interactive Data Language) routines, an Java applet for image decompression (3000 lines), and a Java interface. The package can be used either by calling executables, or by using the C++ classes. Its goal is not to replace existing image processing packages, but to complement them, offering the user a complete set of multiresolution tools. These tools are executable programs, which work on different platforms, outside of any image processing system, and allow the users to perform image operations using multiresolution such as the wavelet transform, filtering, deconvolution, and so on.

The programs, written in C++, are built on three classes: the "image" class, the "multiresolution" class, and the "noise_modeling" class. The "image" class includes routines for reading/writing FITS, MIDAS, GIF, BMP and other images, and a range of standard image processing routines. The "multiresolution" class integrates 24 different multiresolution transforms (orthogonal wavelet transform, à trous algorithms, pyramidal algorithms, non-linear multiresolution transform, and so on). The "noise_modeling" class allows us to determine whether at a given position of the image, and at a given scale, the multiresolution coefficients can be due to noise. Several kinds of noise can be considered (Gaussian noise, Poisson noise, combined Gaussian and Poisson noise, and many others). From these three classes, the multiresolution support of an image can be derived, which is then used by programs for the different applications.

This document presents some results obtained by using multiresolution techniques. More information may obtained at http://visitweb.com/multires, at http://hawk.infm.ulst.ac.uk:1998/multires, and in the book *Image and Data Analysis: The Multiscale Approach* [34].

2 Filtering from the Multiresolution Support

2.1 Introduction

We will say that a multiresolution support of an image describes in a logical or boolean way if an image I contains information at a given scale j and at a given position (x, y). If $M^{(I)}(j, x, y) = 1$ (or $= true$), then I contains information at scale j and at the position (x, y).

Such a support results from the data, the treatment (noise estimation, etc.), and from knowledge of our part of the objects contained in the data (size of objects, linearity, etc.).

The multiresolution support of an image is computed in several steps:

- compute the wavelet transform of the image,

- booleanize each scale, which yields the multiresolution support,

- introduce a priori knowledge by modifying the support

The last step depends on the knowledge we have of our images. For instance, if we know there is no interesting object smaller or larger than a given size in our image, we can suppress, in the support, anything which is due to that kind of object. This can often be done conveniently by the use of mathematical morphology. In the most general setting, we naturally have no information to add to the multiresolution support. In order to visualize the support, we can create an image S defined by:

$$S(x, y) = \sum_{j=1}^{p} 2^j M(j, x, y) \tag{1}$$

The cover figure shows such a multiresolution support visualization of an image of galaxy NGC 2997.

The multiresolution support is obtained by detecting the significant coefficients at each scale. The multiresolution support is defined by:

$$M(j, x, y) = \left\{ \begin{array}{ll} 1 & \text{if } w_j(x, y) \text{ is significant} \\ 0 & \text{if } w_j(x, y) \text{ is not significant} \end{array} \right. \tag{2}$$

where $w_j(x, y)$ are the wavelet coefficients. This implies that we are modeling the noise in the wavelet space [38, 19, 18, 3, 31, 32, 30, 16, 34]. This noise modeling is important because efficiency of the associated applications will depend on how well it is done. The main noise cases include Gaussian, Poisson, and combined Gaussian and Poisson noise. In some cases, we do not know what the noise statistics are, or there are perhaps no known statistics for our data. Then we can always make some assumptions, such as that the noise is locally Gaussian, or carry out a specific study of the noise behavior in wavelet space for a particular type of images.

Iterative methods [19, 31, 30] have been developed in order to restore an image from using its multiresolution support.

2.2   Simulation

A simulated image containing stars and galaxies is shown in Fig. 1 (top left). The simulated noisy image, the filtered image and the residual image are respectively shown in Fig. 1 top right, bottom left, and bottom right. We can see that there is no structure in the residual image. The filtering was carried out using the multiresolution support.
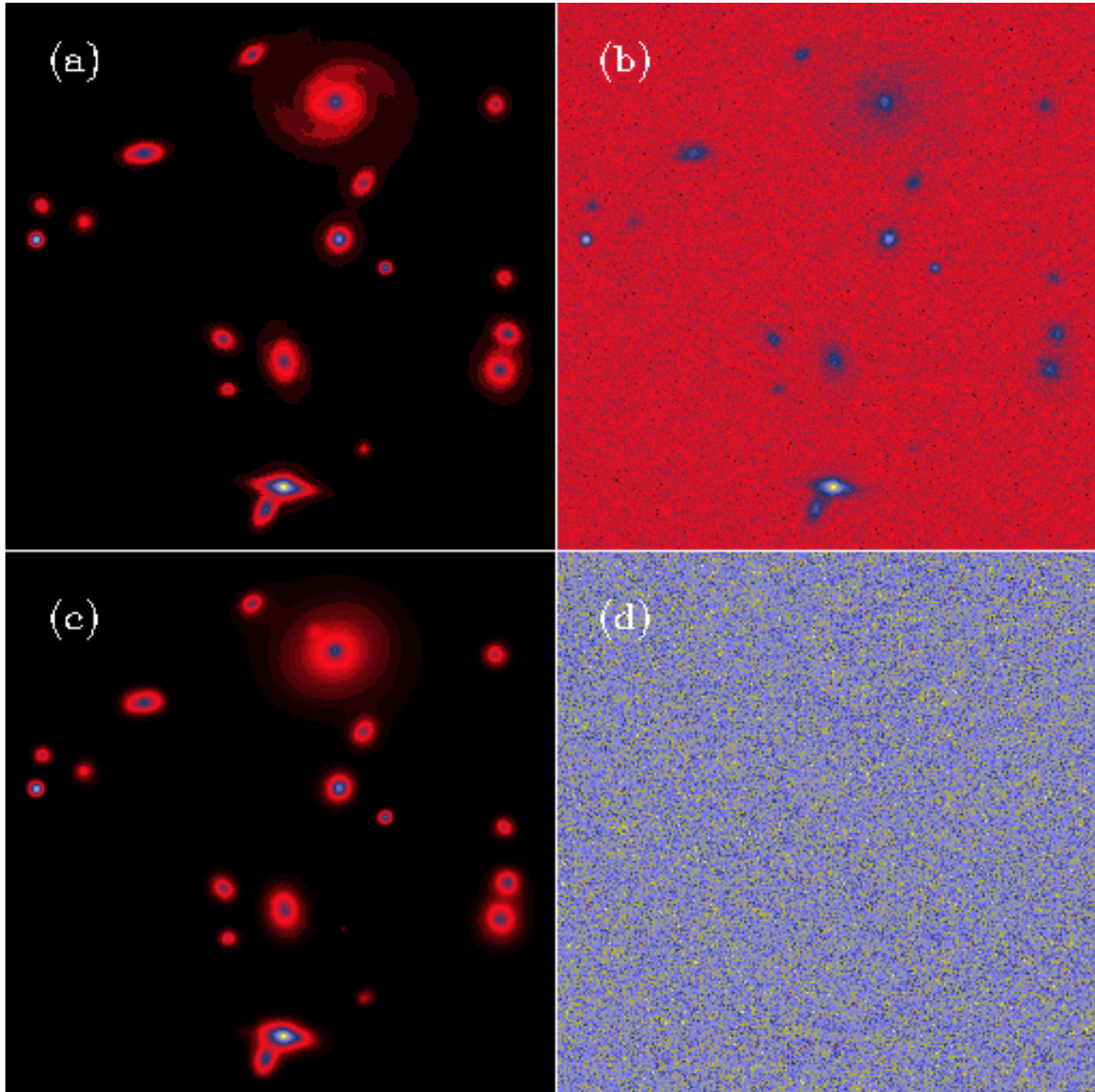

Figure 1: (a) Simulated image, (b) simulated image and Gaussian noise, (c) filtered image, and (d) residual image.

2.3 Spectrum Filtering

Fig. 2 shows a noisy spectrum (upper left, repeated lower right). For the astronomer, the spectral lines –
here mainly absorption lines extending downwards – are of interest. The continuum may also be of interest,
i.e. the overall spectral tendency.

The spectral lines are unchanged in the filtered version (upper center, and upper right). The lower center
(and lower right) version shows the result of applying Daubechies' coefficient 8, a compactly-supported
orthonormal wavelet. This was followed by thresholding based on estimated variance of the coefficients, as
proposed by Donoho [10], but not taking into account the signal's noise properties as we have done [30]. One
sees immediately that a problem- (or image-) driven choice of wavelet and filtering strategy is indispensable.
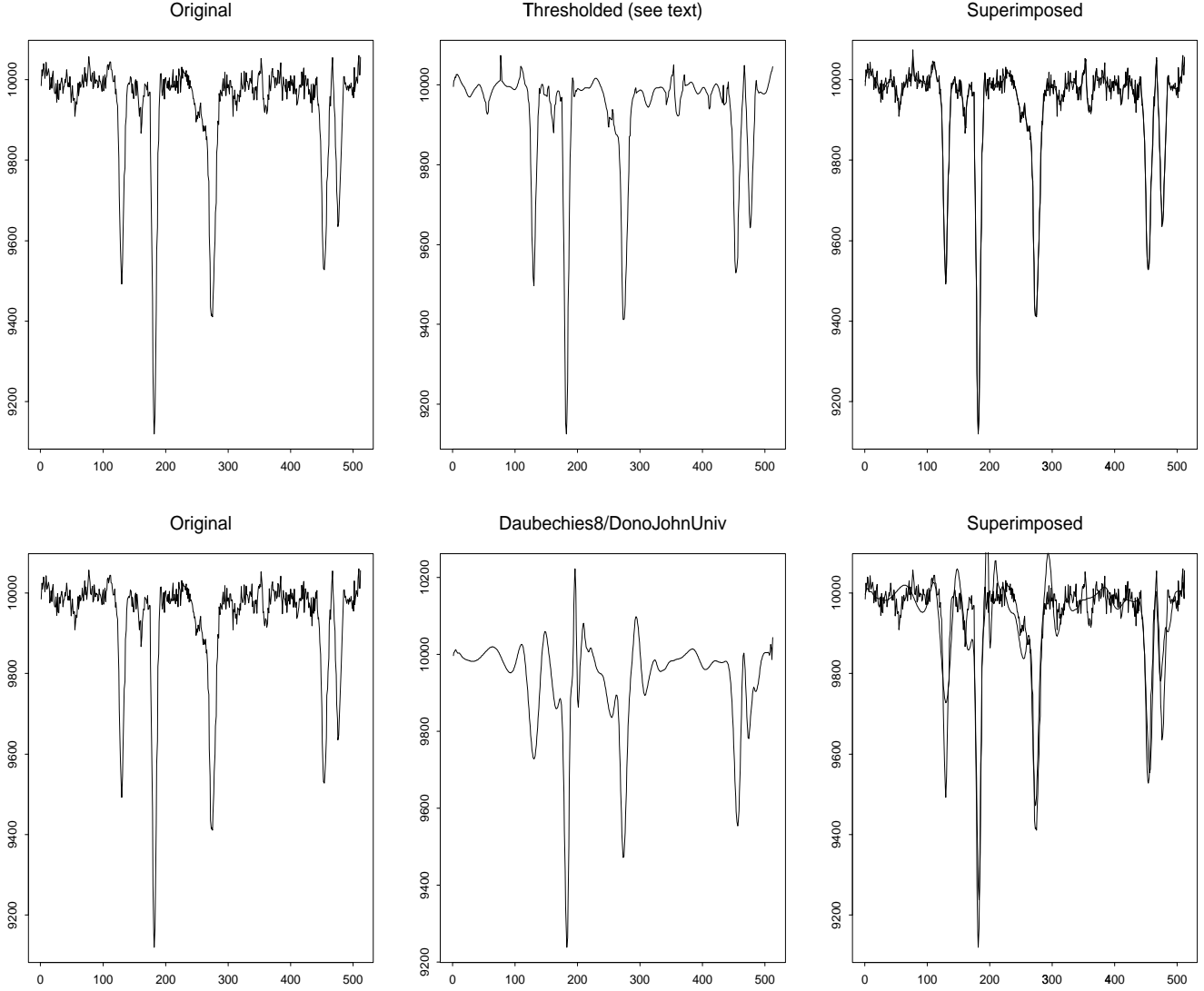

Figure 2: Top row: original noisy spectrum; filtered spectrum using the multiresolution support method; both
superimposed. Bottom row: original; filtered (using Daubechies coefficient 8, and Donoho and Johnstone
"universal" thresholding); both superimposed.

2.4 X-Ray Image Filtering

The galaxy cluster A2390 is at a redshift of 0.231. Figure 3 shows an image of this cluster, obtained by the ROSAT X-ray spacecraft. The resolution is one arcsecond per pixel, with a total number of photons equal to 13506 for an integration time of 8.5 hours. The background level is about 0.04 photons per pixel.

It is obvious that this image cannot be used directly, and some processing must be performed before any analysis. The standard method consists of convolving the image with a Gaussian. Figure 4 shows the result after such a processing. (Gaussian with a full width at half-maximum equal to 5", which is approximatively that of point spread function). The smoothed image shows some structure, but also residual noise, and it is difficult to assign any significance to them.

Figure 5 shows an image filtered by the wavelet transform [37, 17]. The noise has been eliminated, and the wavelet analysis indicates faint structures in X-ray emission, allowing us to explain gravitational amplification phenomena observed in the visible domain [23].
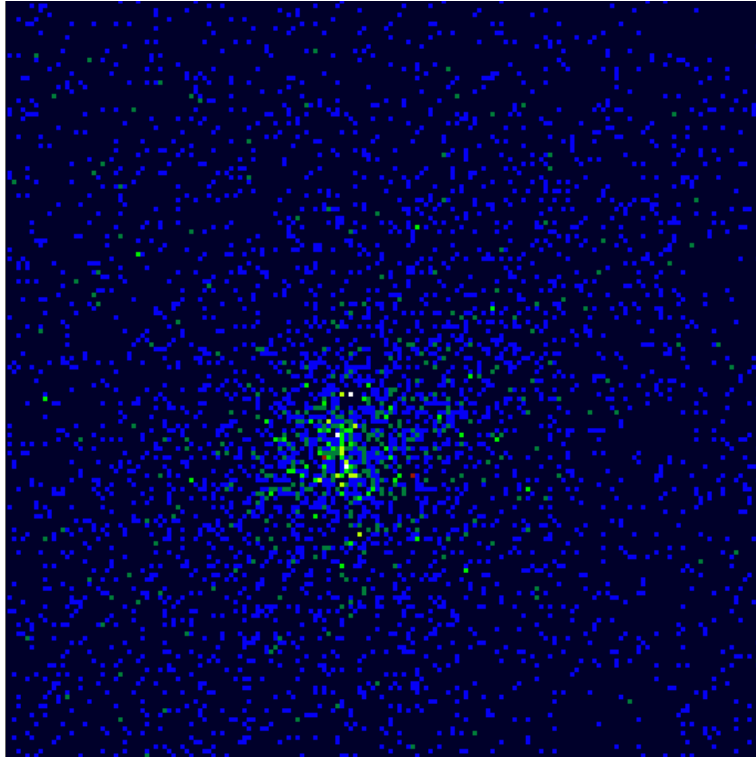

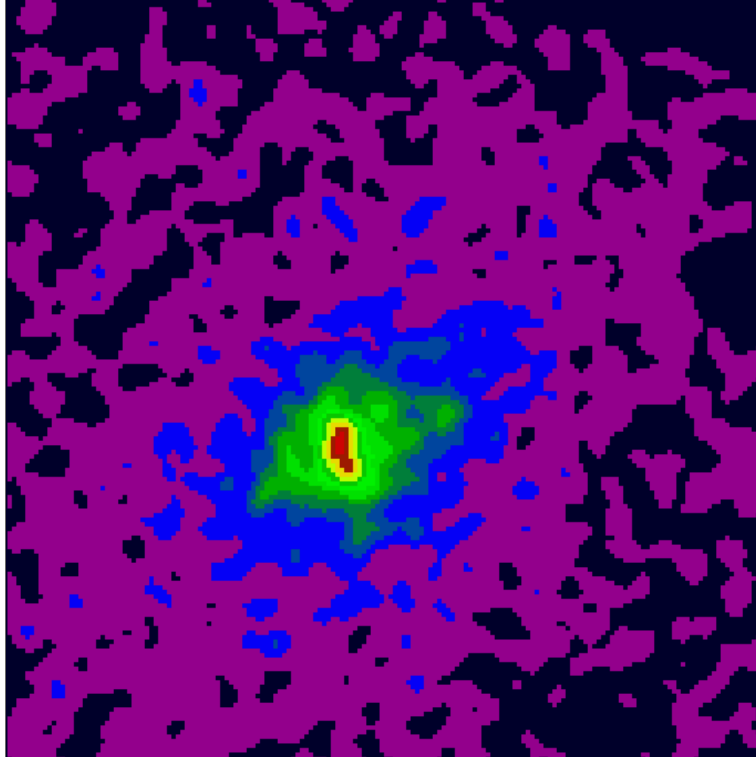Figure 3: ROSAT image of the cluster A2390.

Figure 4: ROSAT image of the cluster A2390 filtered by the standard method (convolution by a Gaussian).
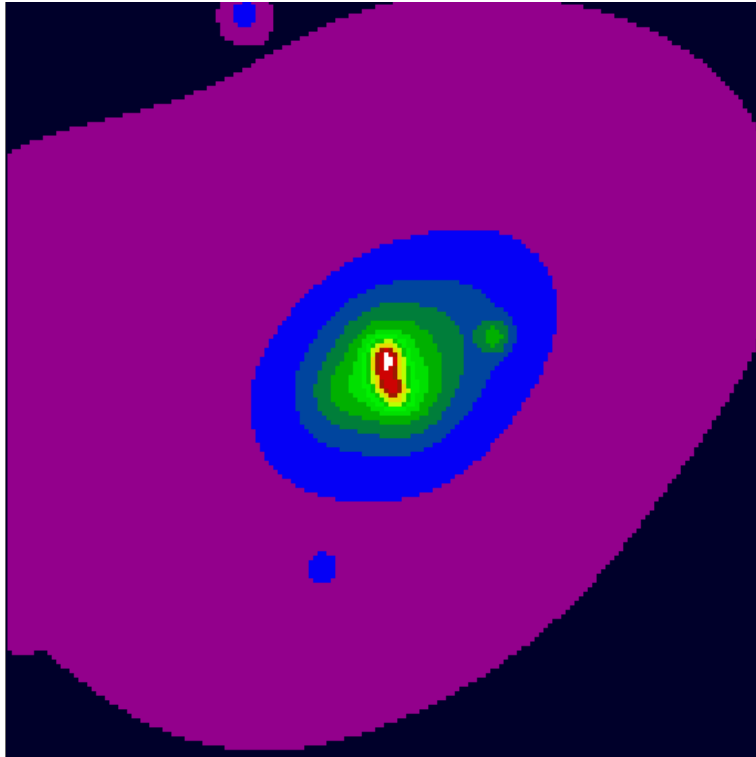

Figure 5: ROSAT image of the cluster A2390 filtered by the method based on wavelet coefficients.

2.5   Mammography Image Filtering

Figure 6 shows a radiological image used in testing for the microcalcifications as symptoms of breast cancer. Information was not available on the image's noise characteristics, and in addition the wispy structures associated with faint tissue provided clutter which made more difficult the process of finding the small local (possibly grouped) points of greater intensity. For these reasons we assumed additive non-homogeneous noise. The pyramidal median transform was used in this case. This was motivated by its robust properties, designed to counteract rather than to faithfully reproduce the faint image features associated with multiple levels of tissue. The iterative multiresolution thresholding approach was used, to refine the initial estimate of the noise. The noise-filtered output image is shown in Figure 7. Smoother structures are evident, as are also the greatly improved candidate set of microcalcifications.
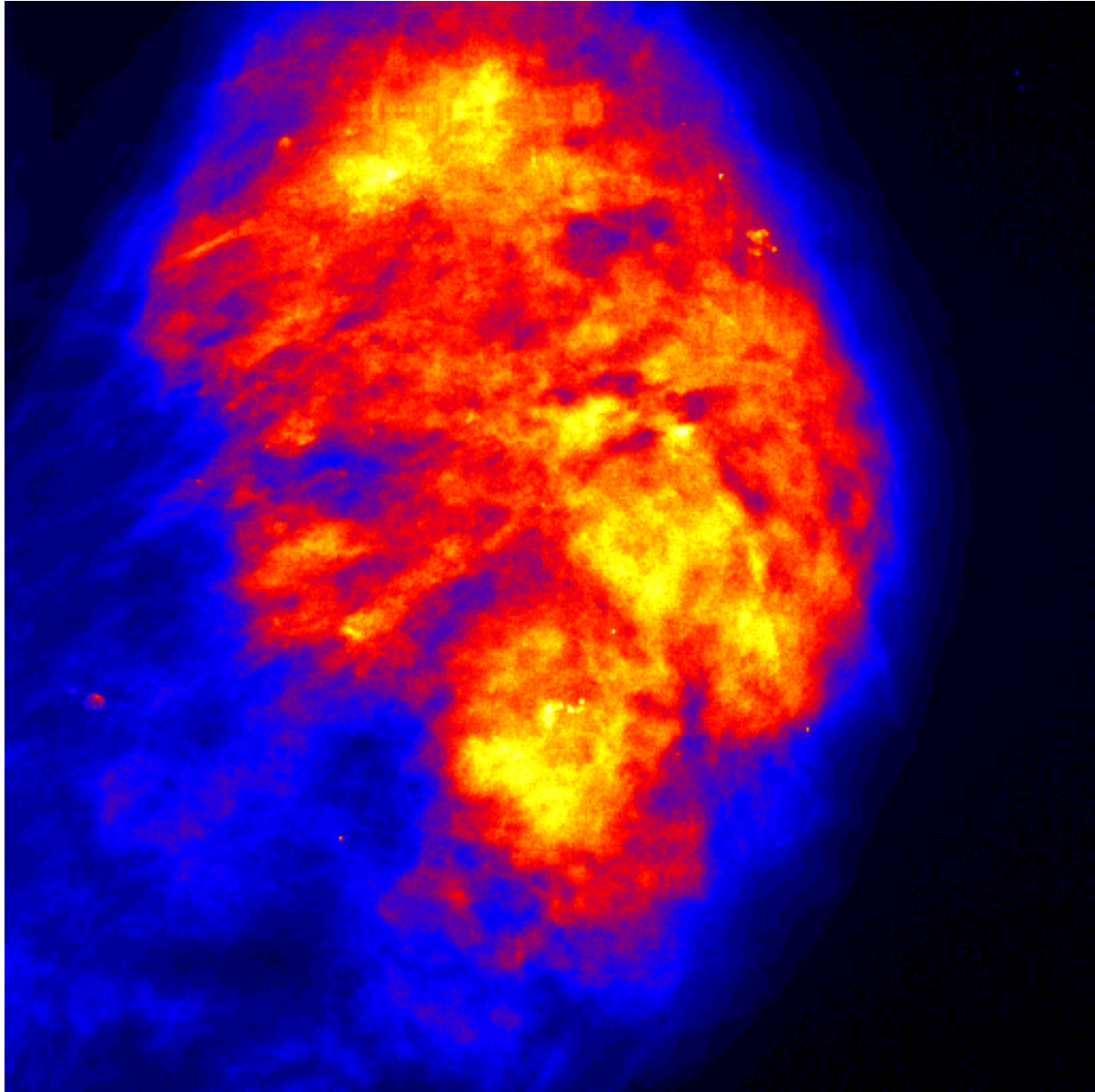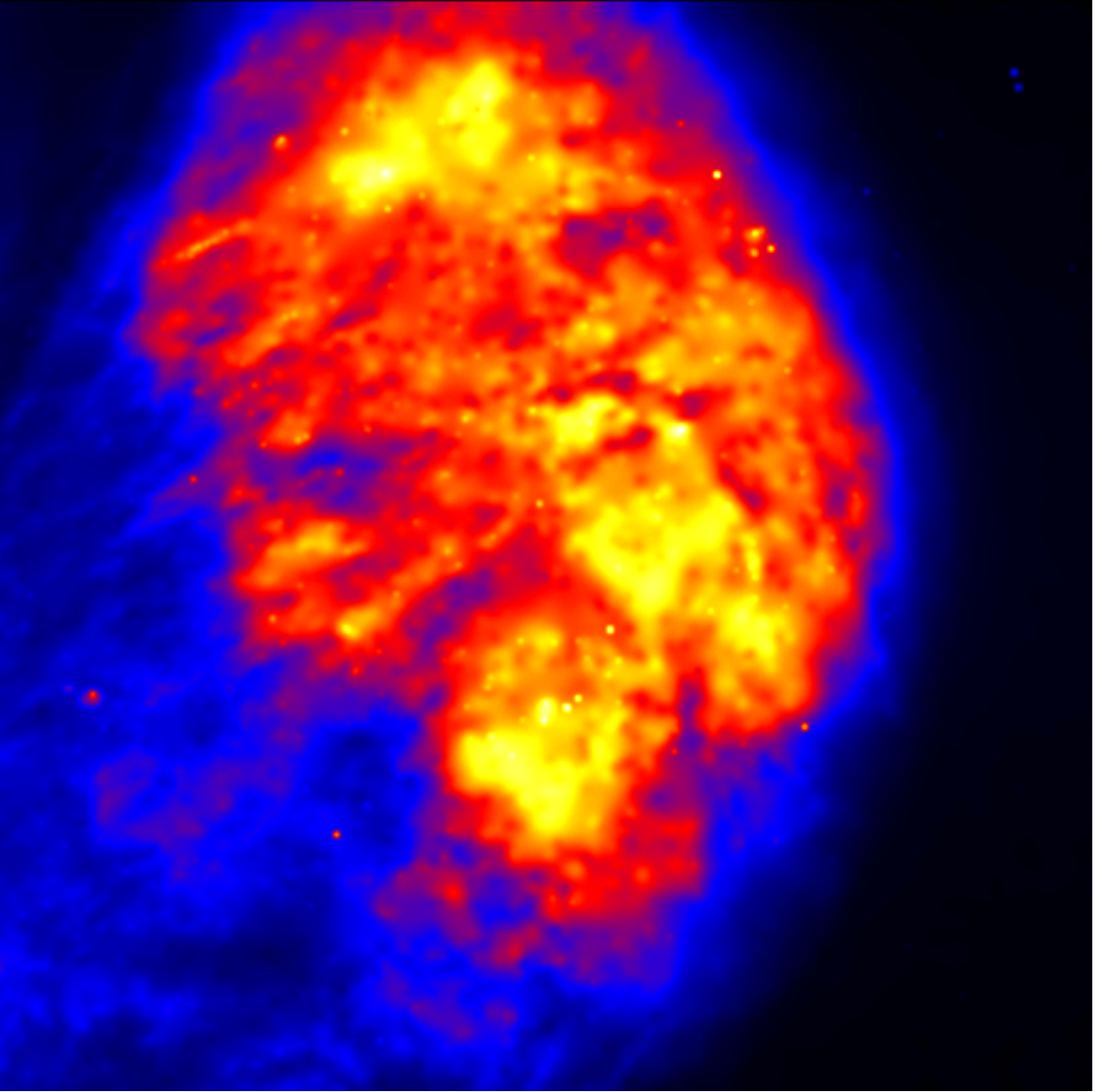

Figure 6: Mammographic image.

Figure 7: Noise-filtered mammographic image.

3 Deconvolution

3.1 Introduction

Observed data Y in the physical sciences are generally corrupted by noise, which is often additive and which follows in many cases a Gaussian distribution, a Poisson distribution, or a combination of both. Using Bayes' theorem to evaluate the probability of the realization of the original signal X, knowing the data Y, we have

$$Prob(X|Y) = \frac{Prob(Y|X).Prob(X)}{Prob(Y)} \tag{3}$$

$Prob(Y|X)$ is the conditional probability of getting the data Y given an original signal X, i.e. it represents the distribution of the noise.

The denominator in equation (3) is independent of X and is considered as a constant (stationary noise). $Prob(X)$ is the a priori distribution of the solution X. In the absence of any information on the solution X except its positivity, a possible course of action is to derive the probability of X from its entropy. Several definitions of entropy has been proposed, and the main ones are:

- Burg [5]: $H_b(X) = -\sum_{pixels} \ln(X)$

- Frieden [11]: $H_f(X) = -\sum_{pixels} X \ln(X)$

- Gull and Skilling [12]: $H_g(X) = \sum_{pixels} X - M - X \ln(X|M)$

Each of these entropies can be used, and they correspond to different probability distributions that one can associate with an image [21]. The final definition of the entropy above has the advantage of having a zero maximum when X equals the model M, usually taken as a flat image. All of these entropy measures are negative, and maximum when the image is flat. They are negative because an offset term is omitted which has no impact on the final solution. The fact that we consider that a signal has maximum information value when it is flat is evidently a curious way to measure information (at least from a physical point of view).

It has been shown [21] that results vary strongly with the background level, and that these entropy functions produce poor results for negative structures, i.e. structures under the background level (absorption area in an image, absorption band in a spectrum, etc.), and compact structures in the signal. The Gull and Skilling entropy gives rise to the difficulty of estimating a model. Furthermore it has been shown [4] that the solution is dependent on this choice.

Many studies [39, 40, 4, 22] have been carried out in order to improve the functional to be minimized. But the question which should be raised is: what is a good entropy measure for signal restoration?

Trying to answer this corresponds to asking what is the information in the signal. The entropy should verify the following criteria [35]:

1. The information in a flat signal is zero.

2. The amount of information in a signal is independent of the background.

3. The amount of information is dependent on the noise. A given signal Y ($Y = X + N$) doesn't furnish the same information if the noise N is high or small.

4. The entropy must work in the same way for a pixel which has a value $B + \epsilon$ (B being the background), and for a pixel which has a value $B - \epsilon$.

5. The amount of information is dependent on the correlation in the signal. If a signal S presents large features above the noise, it contains a lot of information. By generating a new set of data from S, by randomly taking the pixel values in S, the large features will evidently disappear, and this new signal will contain less information. But the pixel values will be the same as in S.

The Burg and Frieden entropy functions do not verify any of these points, and Skilling one verifies one the point 2. The Shannon one, which is derived from the histogram of the data, and has never been used for restoration, verifies the first four points. The main reasons why it has not been used are due to the error introduced by the histogram bin in low flux observations, and to the difficulties posed by introducing histograms into the equations. Using the wavelet transform, it has been shown [35, 33] that an entropy function verifying all cited properties can be derived, which produces good results.

3.2 Simulation

The simulation consists of a faint extended object (galaxy) near a bright star (Figure 8 upper left). This was blurred using a Gaussian point spread function, and noise was added (Figure 8 upper right): the two objects are overlapping and the galaxy is barely detectable. After filtering by the multiscale method (Figure 8 bottom left), an extended object can be clearly identified, but both objects are still overlapping. After deconvolution using the multiscale entropy method (Figure 8 bottom right), the two objects are separated.

It is clear in this example that photometric measurements cannot always be made directly on the data, and deconvolution is often necessary, especially when objects are overlapping.
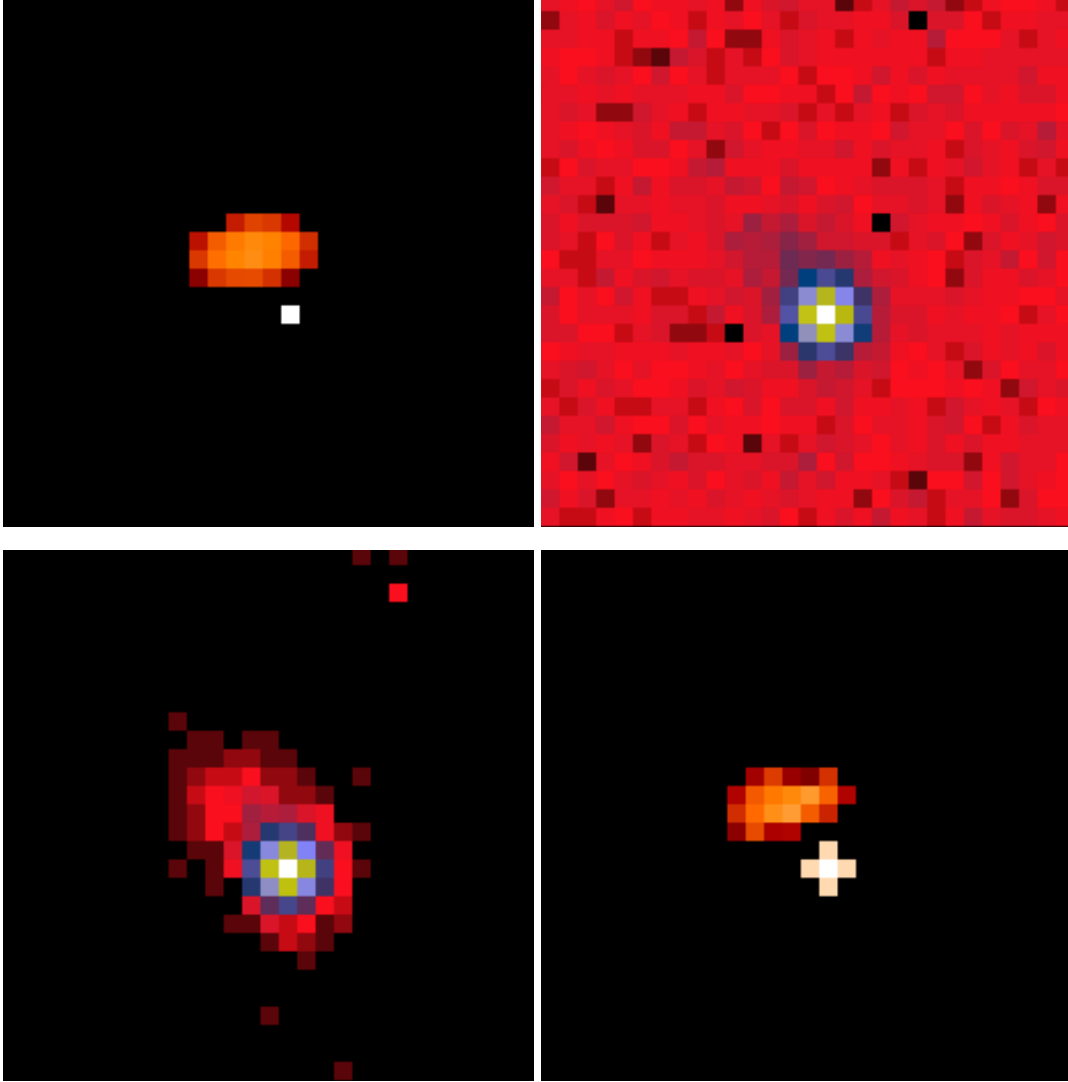

Figure 8: Upper left: original image; upper right: blurred image and noise; bottom left: filtered image; bottom right: deconvolved image.
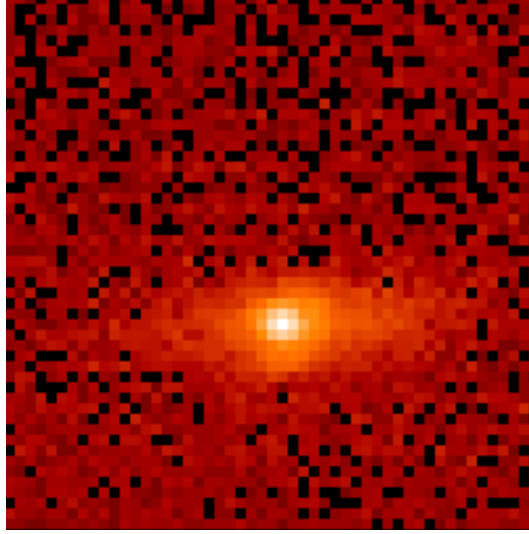
3.3 Beta Pictoris Deconvolution

Figure 9: Beta Pictoris raw data.

The Beta Pictoris image [22] was obtained by integrating 5 hours on-source using an mid-infrared camera, TIMMI, placed on the 3.6 ESO telescope (La Silla, Chile). The raw image has a peak signal-to-noise ratio of 80. It is strongly blurred by a combination of seeing, diffraction (0.7 arcsec on a 3m class telescope) and additive Gaussian noise. The initial disk shape in the original image has been lost after the convolution with the point spread function. Thus we need to deconvolve such an image to get the best information on this object i.e. the exact profile and thickness of the disk, and subsequently to compare the results to models of thermal dust emission.
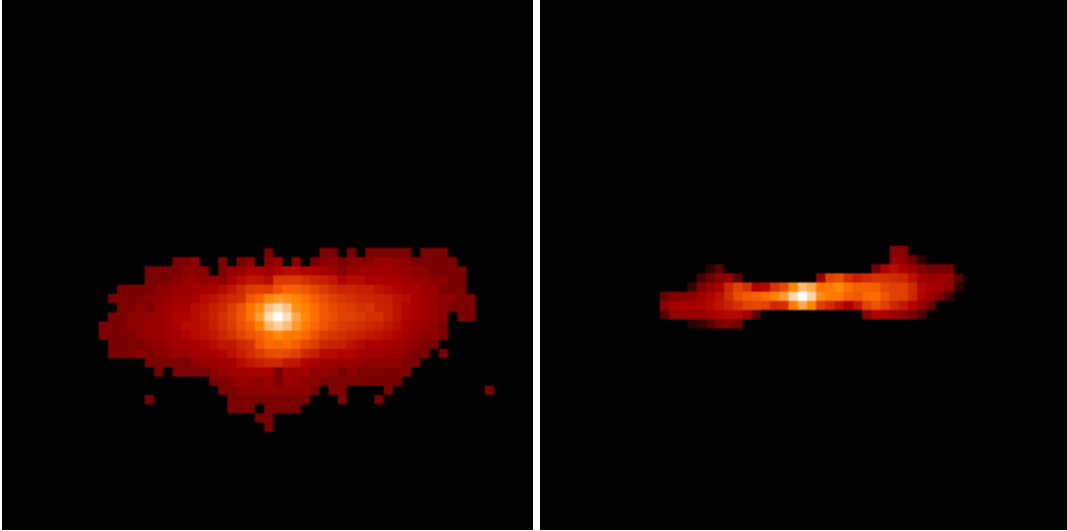
Figure 10: Filtered image (left), and deconvolved one (right).

After filtering (left), the disk appears clearly. For detection of faint structures (the disk here), one can calculate that the application of such a filtering method to this image provides a gain of observing time of a factor of around 60. The deconvolved image (right) shows that the disk is extended at 10 μm and asymmetrical. The multiscale entropy method is more effective for regularizing than other standard methods, and leads to good reconstruction of the faintest structures of the dust disk.

4   Interferometry

Speckle interferometry observations providing an incomplete Fourier plane coverage were successfully processed in [29]. The Multiresolution CLEAN method appears to be well adapted to the analysis of future long baseline interferometry data which are expected to fill irregularly the Fourier plane.

Hen 1379 is a post-Asymptotic Giant Branch star in a phase of intense mass loss. The circumstellar dust distribution for post-AGB generally departs from spherical geometry. This is the case for Hen 1379, the high polarization measured at visible and near-infrared wavelengths indicating that the envelope is strongly non-spherical.
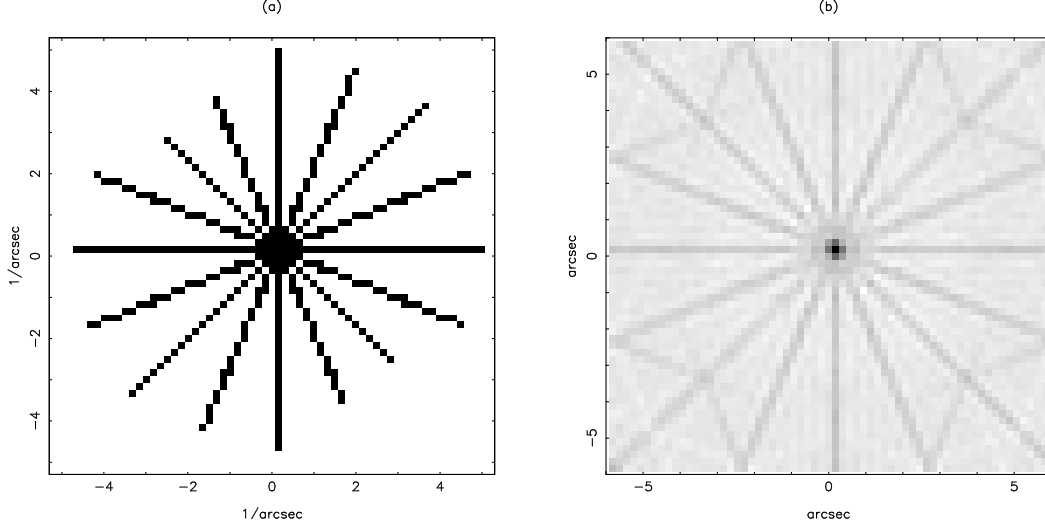

Figure 11: Right, uv plane coverage of Hen 1379, and left, the inverse Fourier transform of the data.
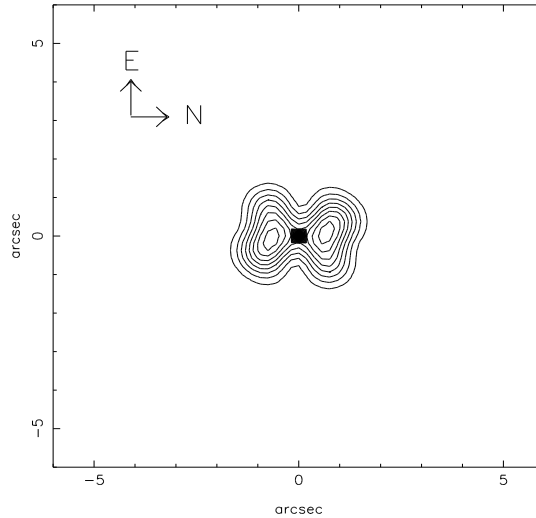
Figure 12: Hen 1379: reconstructed image.

Figure 11 shows the uv plane coverage of Hen 1379, and the inverse Fourier transform of the data. The high angular resolution observations of this source were performed using the ESO one-dimensional (1D) slit-scanning near-infrared specklegraph attached to the ESO 3.6m telescope Cassegrain focus.

Figure 12 shows the reconstruction by the wavelet transform of the evolved star Hen 1379. The ratio of point-source to the maximum amplitude of the envelope is 290. Contour levels are 12, 24, 36, ..., 96% of the maximum amplitude of the envelope.

5 Astronomical Image Compression by the Pyramidal Median Transform

5.1 Introduction

The median transform is nonlinear, and offers advantages for robust smoothing (i.e. the effects of outlier pixel values are mitigated). The multiresolution median transform consists of a series of smoothings of the input image, with successively broader kernels. Each successive smoothing provides a new resolution scale. The multiresolution coefficient values constructed from differencing images at successive resolution scales are not necessarily of zero mean, and so the potential artifact-creation difficulties related to this aspect of wavelet transforms do not arise.

For integer input image values, this transform can be carried out in integer arithmetic only which may lead to computational savings. Computational requirements of the multiresolution median transform are high, and these can be reduced by decimation: one pixel out of two is retained at each scale. In the Pyramidal Median Transform (PMT), the kernel or mask used to obtain the succession of resolution scales remains the same at each level. The image itself, to which this kernel is applied, becomes smaller. While this algorithm aids computationally, the reconstruction formula for the input image is no longer immediate. Instead an algorithm based on B-spline interpolation can be used for reconstruction.

The principle of the compression method is to select the information we want to keep, by using the PMT, and to code this information without any loss. Thus the first phase searches for the minimum set of quantized multiresolution coefficients which produce an image of "high quality". The quality is evidently subjective, and we will define by this term an image such as the following:

- There is no visual artifact in the decompressed image.

- The residual (original image minus decompressed image) does not contain any structure.

Lost information cannot be recovered, so if we do not accept any loss, we have to compress what we take as noise too, and the compression ratio will be low (3 or 4 only). The method employed involves the following sequence of operations:

1. Determination of the multiresolution support.

2. Determination of the quantized multiresolution coefficients which give the filtered image.

3. Coding of each resolution level using the Huang-Bijaoui method [13]. This consists of quadtree-coding each image, followed by Huffman-coding the quadtree representation. There is no information lost during this phase.

4. Compression of the noise if this is wished.

5. Decompression consists of reconstituting the noise-filtered image (plus the compressed noise if this was specified).

The decompression is carried out scale by scale, starting from the low resolution, so it is not necessary to decompress the entire file if one is just interested in having a look at the image. Noise is decompressed and added at the end, if this is wanted. See the full description of the method in [36].
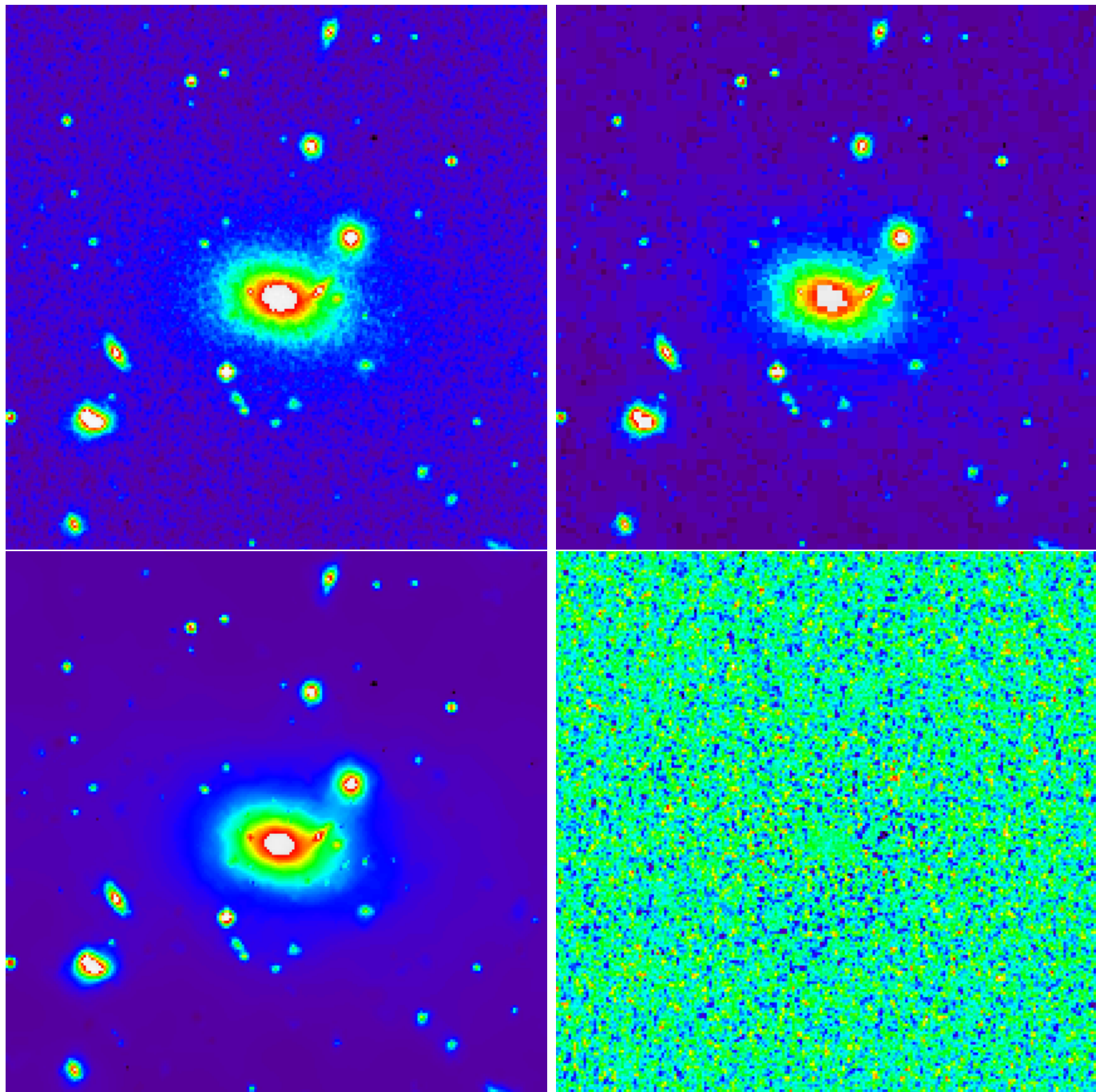
5.2 Example 1: Comparison with HCOMPRESS

Figure 13: Upper left, Coma cluster from a Space Telescope Science Institute POSS-I digitized plate. Upper right, decompressed image using HCOMPRESS (30:1). Bottom left, decompressed image using Pyramidal Median Transform (30:1). Bottom right, difference between the original image and the PMT decompressed one.

5.3 Example 2: Comparison with JPEG

5.3.1 Visual Quality

Figure 14 shows a subimage of a Schmidt photographic plate of the region of M5 (numbered ESO 7992v). This photographic plate was digitized using the MAMA ("Machine Automatique à mesurer pour l'Astronomie") machine of Paris Observatory (Paris, France).

For the two compression methods studied here, each implying loss of information, we have to look for a good compromise between compression rate and visual quality.

In the case of JPEG, various studies confirm that beyond a compression rate of 40 this method of compression, when used on 16 bit/pixel images, gives rise to 'blocky' artifacts.

For the Pyramidal Median Transform (PMT) [36, 20, 15], the reconstruction artifacts appear at higher compression rates, beyond a rate of 260 in the particular case of our images. Figures 15 et 16 allow the visual quality of both the JPEG and PMT to be compared.
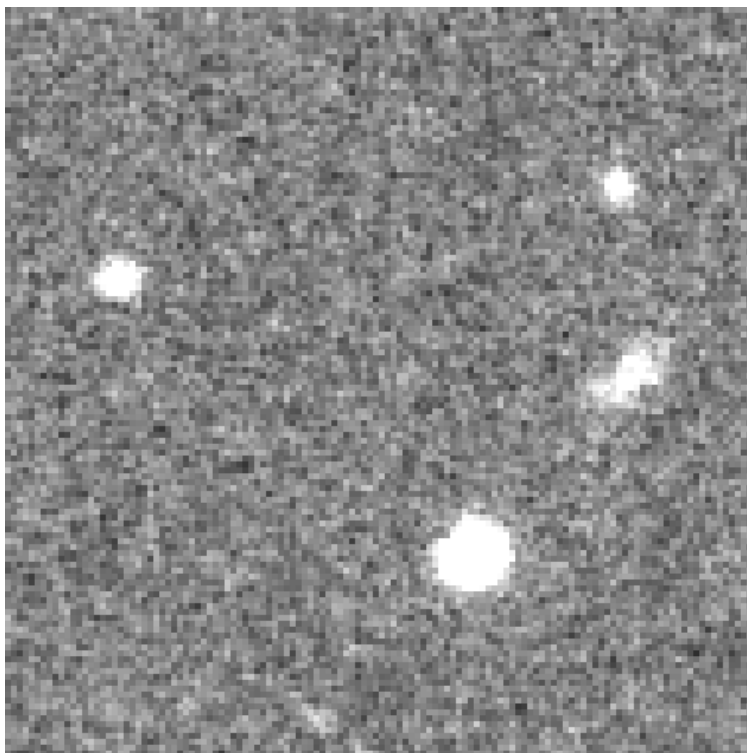

Figure 14: Original image: subimage extracted from 1024x1024 patch, extracted in turn from the central region of ESO7992v.
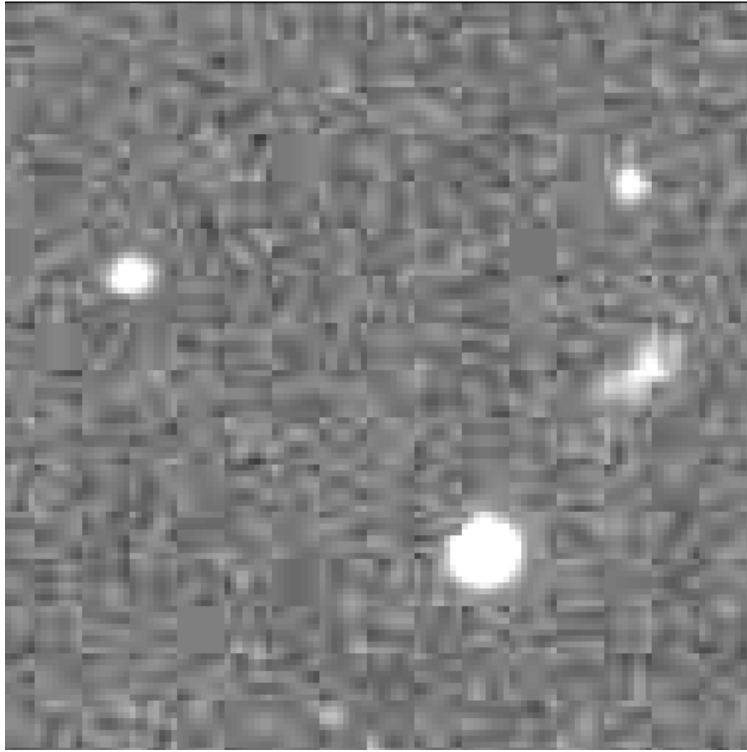
Figure 15: JPEG compressed image at 40:1 compression rate: small image patch extracted from central region of ESO7992v.
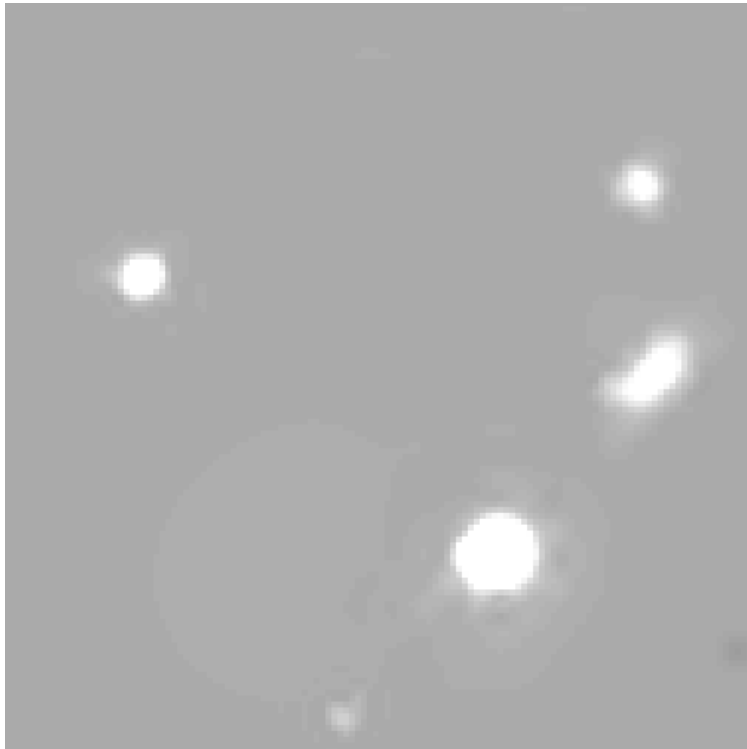

Figure 16: PTM compressed image at 260:1 compression rate: small image patch extracted from central region of ESO7992v.

5.3.2   Photometry – Intensity-Related Quality

We measure the photometric stability of the objects following compression, relative to their representation in the original image. The corresponding error curves are shown in Figures 17 and 18.
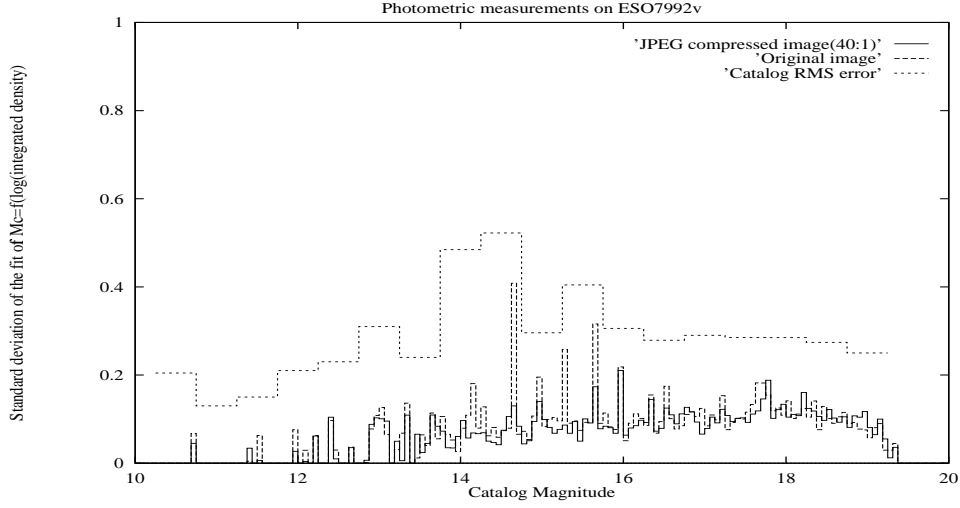

Figure 17: Comparison of the calibration error, by 0.0625 magnitude intervals, between the uncompressed image using JPEG, the original image, and the reference catalog.
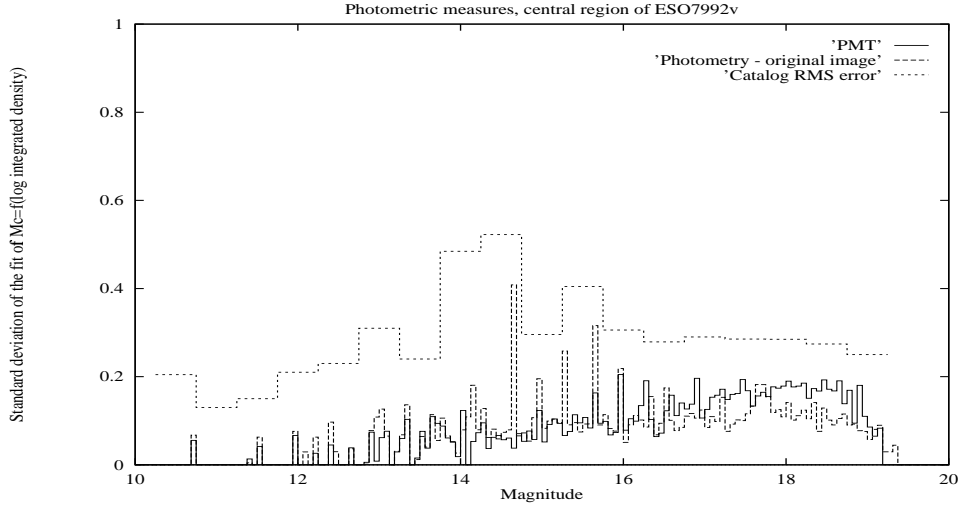
Figure 18: Comparison of the calibration error, by 0.0625 magnitude intervals, between the uncompressed image using PMT, the original image, and the reference catalog.

The JPEG curve shows a slight increase for magnitudes above 18, and a smoothing effect for brighter objects between 14 and 16.

For PMT, an increase in dispersion is noticed for high magnitudes, which corresponds to the problem of the detection of faint objects. We note that the number of intervals below 14 is too small to allow for interpretation of the behavior of very bright objects.

Even if PMT brings about greater degradation in the photometry of objects, especially when the objects are faint, the errors stay close to that of the catalog, and as such are entirely acceptable. Of course we recall also that the compression rate used with PMT is 260:1, compared to 40:1 for JPEG.

5.3.3 Astrometry – Positional Quality

To estimate the influence of compression algorithms on astrometrical precision, a set of objects was studied [20], and it was shown [20] that the error is below the systematic error of the catalog, in particular in the interval from object magnitudes 13 to 19 where we have sufficient objects to warrant asserting a significant result. Outside that interval, our dataset does not contain enough objects to establish a mean error in the astrometry.

Figure 19 allows the performances of JPEG and PMT to be compared.
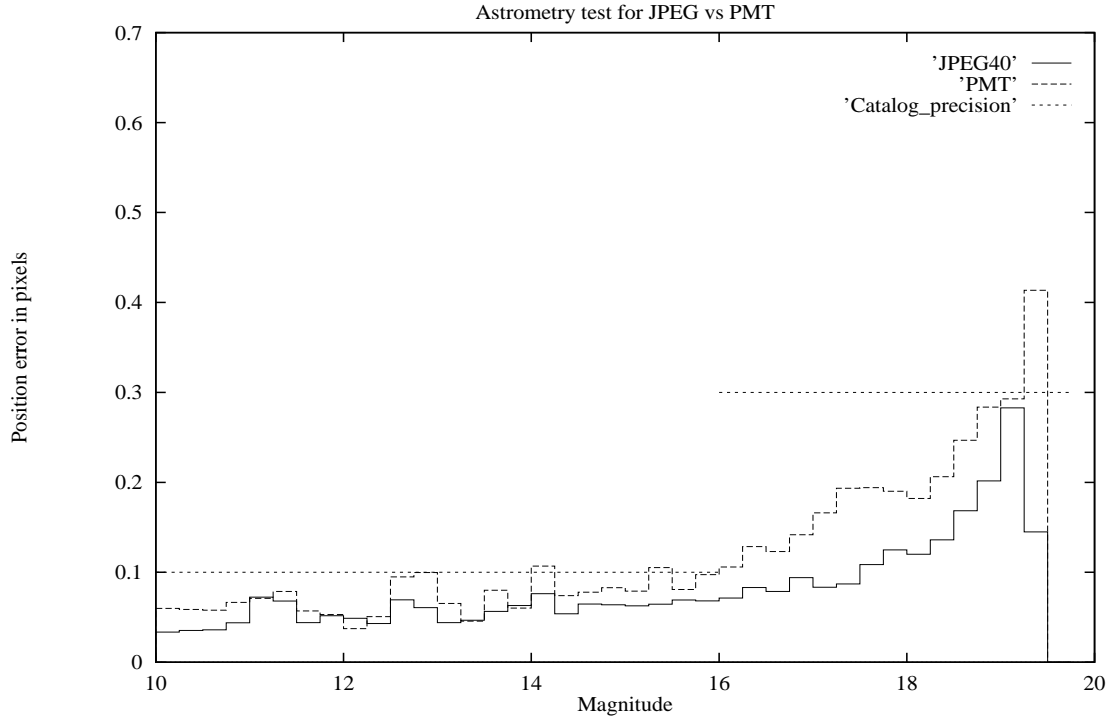
Figure 19: Mean error in astrometry, by interval of 0.25 magnitude, for images compressed 40 times by JPEG and 260 times by PMT.

5.4 Conclusion

The PMT method provides impressive compression rates, coupled with acceptable visual quality. It is robust and can allow for certain image imperfections. On an Ultra Sparc 1 workstation, compressing a 900×900 image takes about 6 seconds (CPU time), with subsequent very fast decompression.

The decomposition of the image into a set of resolution scales, and furthermore the fact they are in a pyramidal data structure, can be used for effective transmission of image data. Current work on World-Wide Web progressive image transmission capability has used bit-plane decomposition . Using resolution-based and pyramidal transfer and display with WWW-based information transfer is a further step in this direction.

6 Image Registration

6.1 Introduction

Image registration is a procedure that determines the best spatial fit between two or more images that overlap the same scene, acquired at the same or at a different time, by identical or different sensors. Thus, image registration is required to process the new set of data in such a way that its image under an appropriate transform is in proper geometrical registration with the previous set of data.

Several digital techniques have been used for automatic registration of images such as cross-correlation, normal cross-correlation and minimum distance criteria for example [1] [14] [24]. Automatic registration of remotely sensed data based on the multiresolution decomposition of the data with the use of the wavelet transform has been developed [8, 9]. The advantage of the wavelet transform is that it produces both spatial and frequency domain information which allows the study of the image by frequency bands.

An automatic image registration procedure can be helpful for several applications:

1. Comparison between two images obtained at the same wavelength.

2. Comparison between two images obtained at different wavelength.

3. Pixel field of view distortion estimation.

The geometrical correction is usually performed by three operations [24]:

- The measure of a set of well defined ground control points (GCPs), which are features well located both in the input image and in the reference image.

- The determination of the warping or deformation model, by specifying a mathematical deformation model defining the relation between the coordinates (x, y) and (X, Y) in the reference and input image respectively.

- The construction of the corrected image by output-to-input mapping.

The main difficulty lies in the automated localization of the corresponding GCPs, since the accuracy of their determination will affect the overall quality of the registration. In fact, there are always ambiguities in matching two sets of points, as a given point corresponds to a small region D, which takes into account the prior geometric uncertainty between the two images and many objects could be contained in this region.

One property of the wavelet transform is to have a sampling step proportional to the scale. When we compare the images in the wavelet transform space, we can choose a scale corresponding to the size of the region D, so that no more than one object can be detected in this area, and the matching is done automatically.

6.2   Application to SPOT images

The two SPOT scenes we worked on are:

- Scene number 51 – 279 dated 18/05/1989 taken at $10h\_48mn\_10s$, composed of 3005 rows and 3270 columns.

- Scene number 51 – 279 dated 12/05/1986 taken at $10h\_41mn\_28s$, composed of 3003 rows and 3253 columns.

These scenes, from the region of Ain Ousseira in Algeria, were taken with a three-year time interval, in a region subject to desertification, and are therefore radiometrically very different as one can easily see. Two sub-scenes of 750×750 pixels where extracted in the XS1 $(0.5 - 0.59\mu m)$, XS2 $(0.61 - 0.68\mu m)$ and XS3 $(0.79 - 0.89\mu m)$.

Our registration algorithm was then applied to the selected subimages, using the scene of 1986 as the reference one (Figure 20) and the one of 1989 as the image to be registered (Figure 21). The processing was done using a six-level wavelet decomposition and the results are shown for the XS3 band. The resulting registration is given in Figure 22.
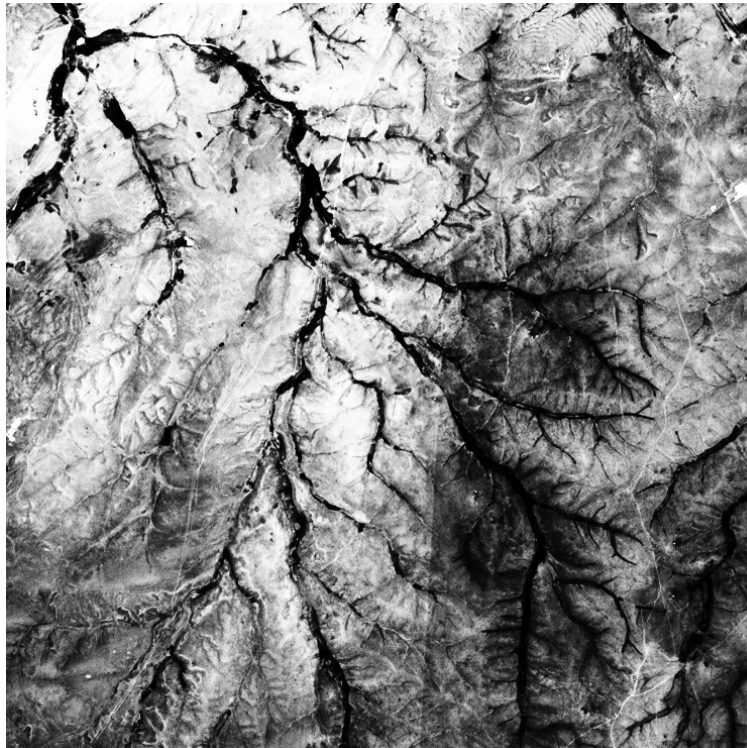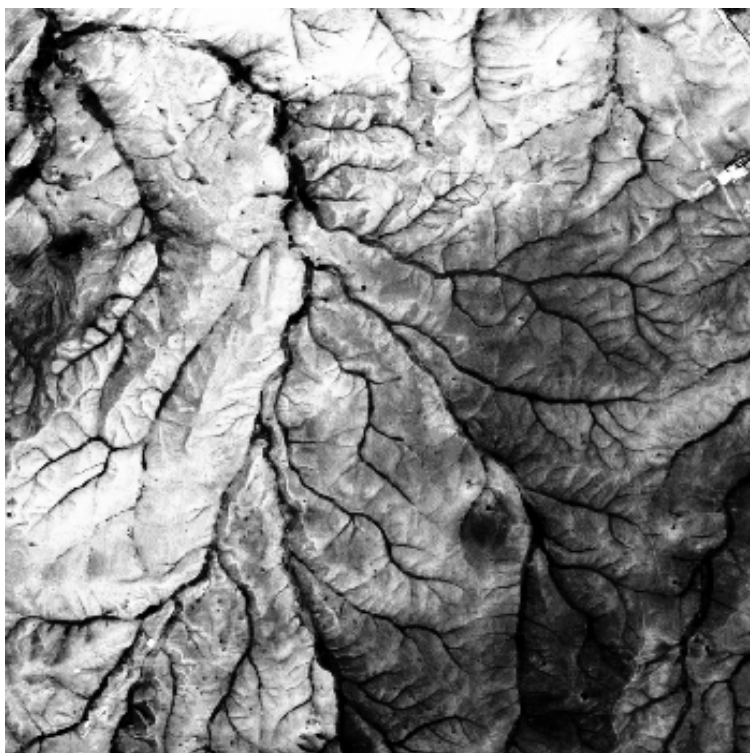

Figure 20: The SPOT XS3 reference image.

Figure 21: The SPOT XS3 working image.

Figure 22: The SPOT XS3 corrected image.

7 Object Detection

7.1 Introduction

Astronomical images contain typically a large set of point-like sources (the stars), some quasi point-like objects (faint galaxies, double stars) and some complex and diffuse structures (galaxies, nebulae, planetary stars, clusters, etc.). These objects are often hierarchically organized: star in a small nebula, itself embedded in a galaxy arm, itself included in a galaxy, and so on.

A *vision model* is defined as the sequence of operations required for automated image analysis. Taking into account the scientific purposes, the characteristics of the objects and the existence of hierarchical structures, astronomical images need specific vision models. This is also the case in many other fields, such as remote sensing, hydrodynamic flows or biological studies. Specific vision models have been implemented for these kind of images.

For reducing astronomical images, many procedures have been proposed using a model for which the image is the sum of a slowly variable background with superimposed small-scale objects. A background mapping is first built. For that purpose we need to introduce a scale: the background is defined in a given area. Each pixel with a value significantly greater than the background is considered to belong to a real object. The same label is given to each significant pixel belonging to the same connected field. For each field we determine the area, the position, the flux and some pattern parameters. Generally, this procedure leads to quite accurate measurements, with correct detection and recognition. The model works very well for content-poor fields. If this is not the case, a labeled field may correspond to many objects. The background map is constructed at a given scale. Larger objects are removed. This smoothing is only appropriate for star detection and not for larger objects.

This vision model failed on many sets of images because it is based on a single spatial scale for the adaptive smoothing and for the background mapping.

A multiscale analysis allows us to get a background appropriate to a given object, and to optimize the detection of different sized objects. The wavelet transform is expected to be the tool allowing us to build up an analysis, taking into account all the constraints.

In the Multiscale Vision Model [2], an object in a signal is defined as a set of structures detected in the wavelet space. By using interscale relations, wavelet coefficients are connected together in order to form an object. A structure is defined by a group of connected significant wavelet coefficients. An object is described as a hierarchical set of structures. In order to define this hierarchy, we have to link the labeled fields from a scale to the following one. This interscale relation enables one to build the interscale connectivity graph whose vertices correspond to the labeled field.

Once an object is detected in the wavelet space, we may want to reconstruct it. The problem of reconstruction [2] consists of searching for a signal V such that its wavelet coefficients are the same as those of the detected structure. By noting $\mathcal{T}$ the wavelet transform operator, and P_b the projection operator in the subspace of the detected coefficients (i.e. setting to zero all coefficients at scales and positions where nothing was detected), the solution is found by minimization of

$$J(V) = \| W - (P_b \circ \mathcal{T})\mathcal{V} \| \tag{4}$$

where W represents the detected wavelet coefficients of the signal. A complete description of algorithms for minimization of such a functional can be found in Bijaoui & Rué (1995).
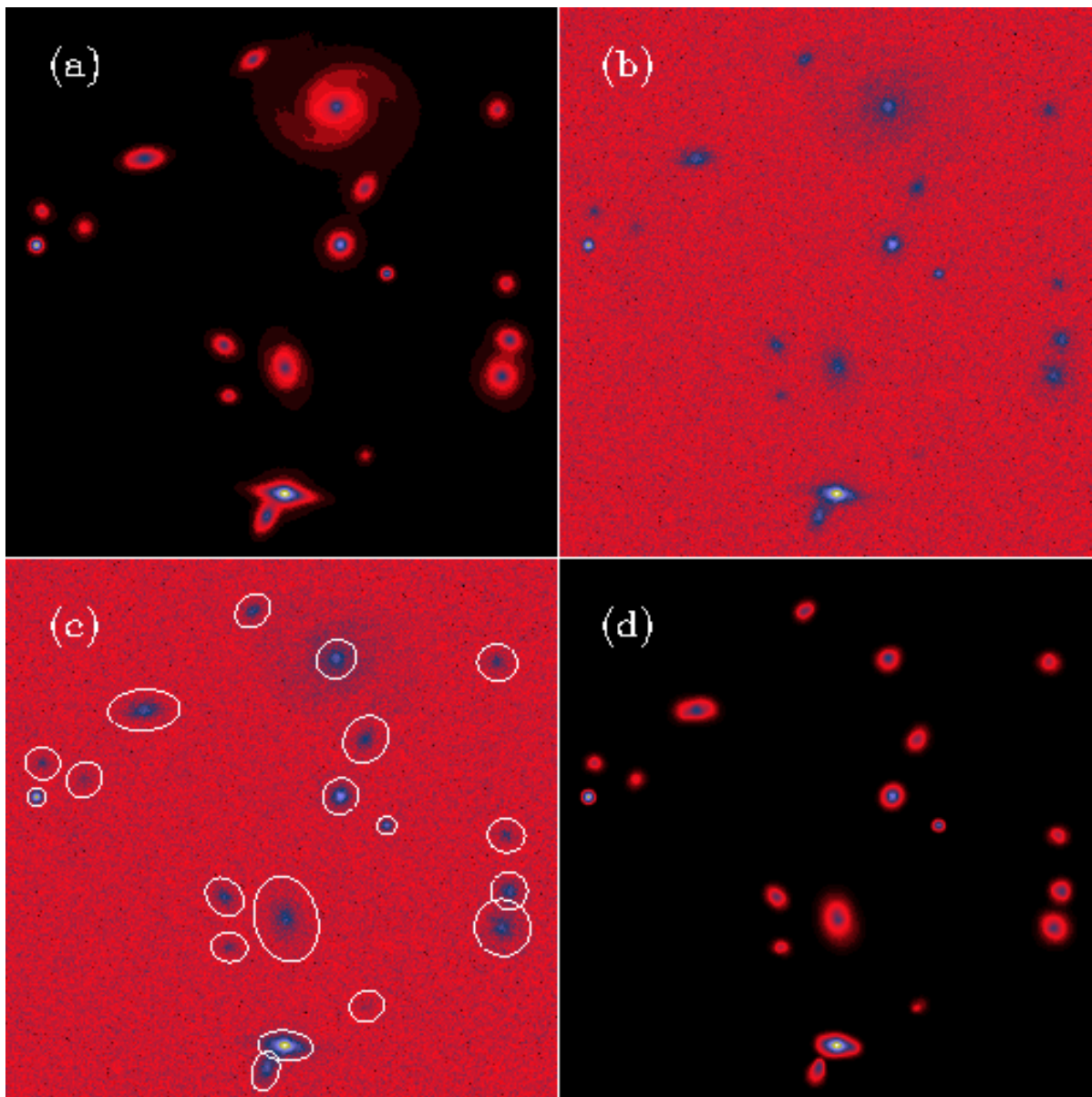
Figure 23: (a) Simulated image, (b) simulated image and Gaussian noise, (c) detected objects, and (d) image built from the reconstructed objects.

7.3 ISOCAM Data Calibration from Pattern Recognition

The ISOCAM infrared camera is one of the four instruments on board the ISO (Infrared Space Observatory) spacecraft which ended its life on May 1998. It operated in the 2.5-17 μm range, and was developed by the ISOCAM consortium lead by the French Service d'Astrophysique of CEA Saclay [6].

The main difficulty in dealing with ISOCAM faint source detection is the combination of the cosmic ray impacts (glitches) and the transient behavior of the detectors [25, 26]. Indeed, for glitches producing a single fast increase and decrease of the signal, a simple median filtering allows a fairly good deglitching, while for other glitches, memory effects can produce false detections. Consequently, the major source of errors here is not the detection limit of the instrument, which is quite low, but the large number of glitches which create false detection.
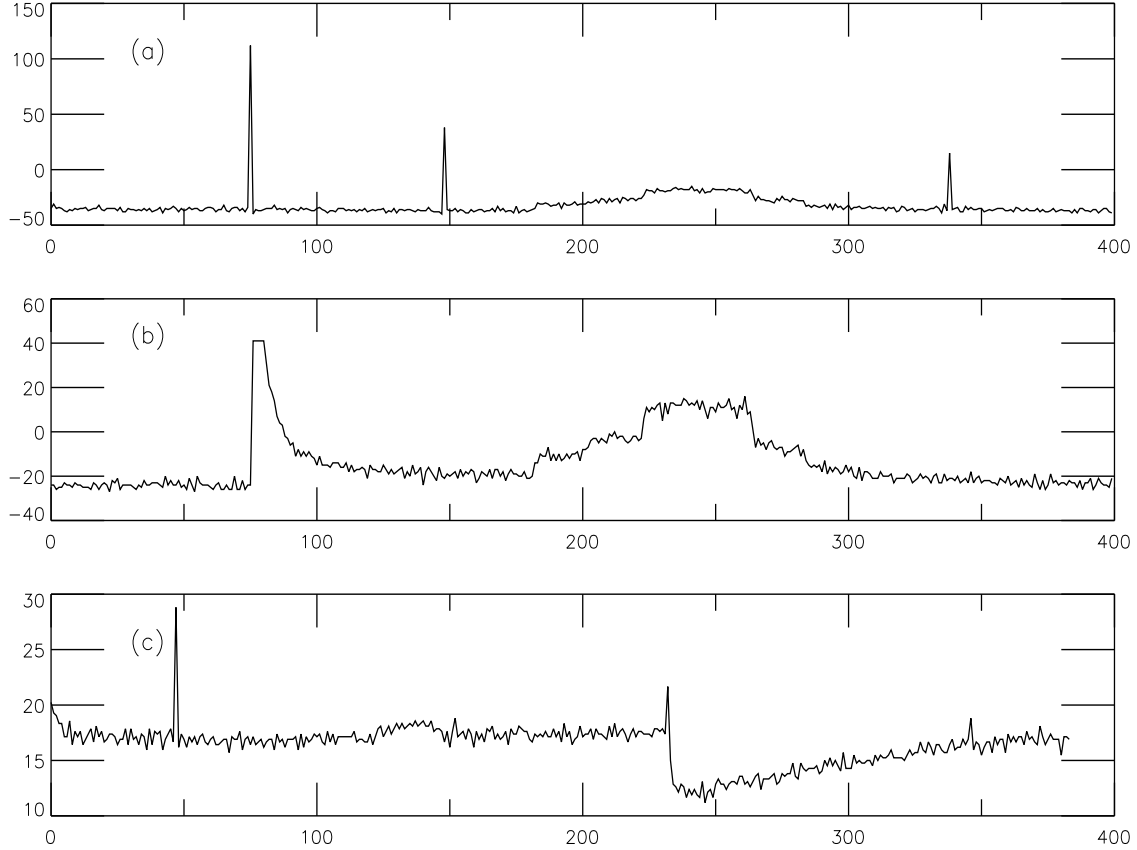

Figure 24: Examples of glitches. (a) This signal contains three glitches of the first type. (b) A glitch with a long tail appears (named fader) around the position 80. The glitch has been truncated, and its real amplitude is 2700 ADUs. (c) A glitch with a negative tail (named deeper) appears around position 240.

Three types of glitches can be distinguished [7]:

- a positive strong and short feature (lasting one readout),
- a positive tail (called *fader*, lasting a few readouts),
- a negative tail (called *dipper*, lasting several tens of readouts).

Figure 24 is a plot of the camera units (ADU, for Analog to Digital Units) measured by a single pixel as a function of the number of readouts, i.e. time, which shows the three types of glitches. On top (a), three sharp type "1" glitches are clearly visible. In the middle plot (b), another pixel history shows a "fader" (at

25

about 80 readouts and lasting about 20 readouts). In the bottom plot (c), a "dipper" is present at readout 230, which lasts about 150 readouts.

Finally, the signal measured by a single pixel as a function of time is the combination of memory effects, cosmic ray impacts and real sources: memory effects begin with the first readouts, since the detector faces a flux variation from an offset position to the target position (stabilization), then appear with long-lasting glitches and following real sources. One needs to clearly separate all these constituents of the signal in each pixel before building a final raster map and to keep the information of the associated noise before applying a source detection algorithm. Indeed, since the glitches do not follow Gaussian statistics, it is clear that an analysis of the final raster map would lead to poor results, for the standard detection criteria (detection above N times the standard deviation of the noise) would no longer be valid.

The calibration from pattern recognition [27, 28] consists of searching only for objects which verify given conditions. For example, finding glitches of the first type is equivalent to finding objects which are positive, strong, and with a temporal size lower than that of the sources.
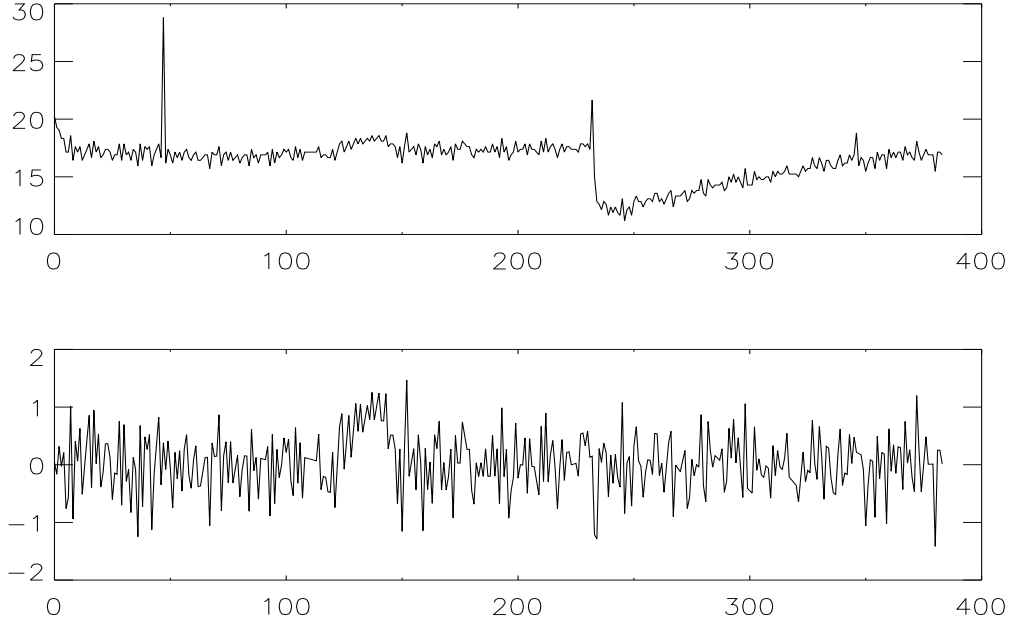

Figure 25: Top, original data, and bottom, calibrated data (background free). The flux in ADUs (Analog to Digital Units) is plotted against time given by the number of exposures. Note the gain variation of about 5 ADUs which appears after the second glitch.

Figure 25 (bottom) presents the result after carrying out such processing. Original data are shown in Figure 25 (top). Figure 26 shows the decomposition of the original signal (see Figure 25 top) into its principal components: (a), (b), and (d) are features (short glitch, glitch negative tail, and baseline) which present no direct interest for faint source detection, and (c) and (e) (source and noise) must be considered further. The noise must also be kept because faint sources could be undetectable in a single temporal signal, but detectable after co-addition of the data. The simple sum of the five components is exactly equal to the original data (see Figure 25 top). The calibrated background free data (see Figure 25 bottom) are then obtained by addition of (c) and (e).
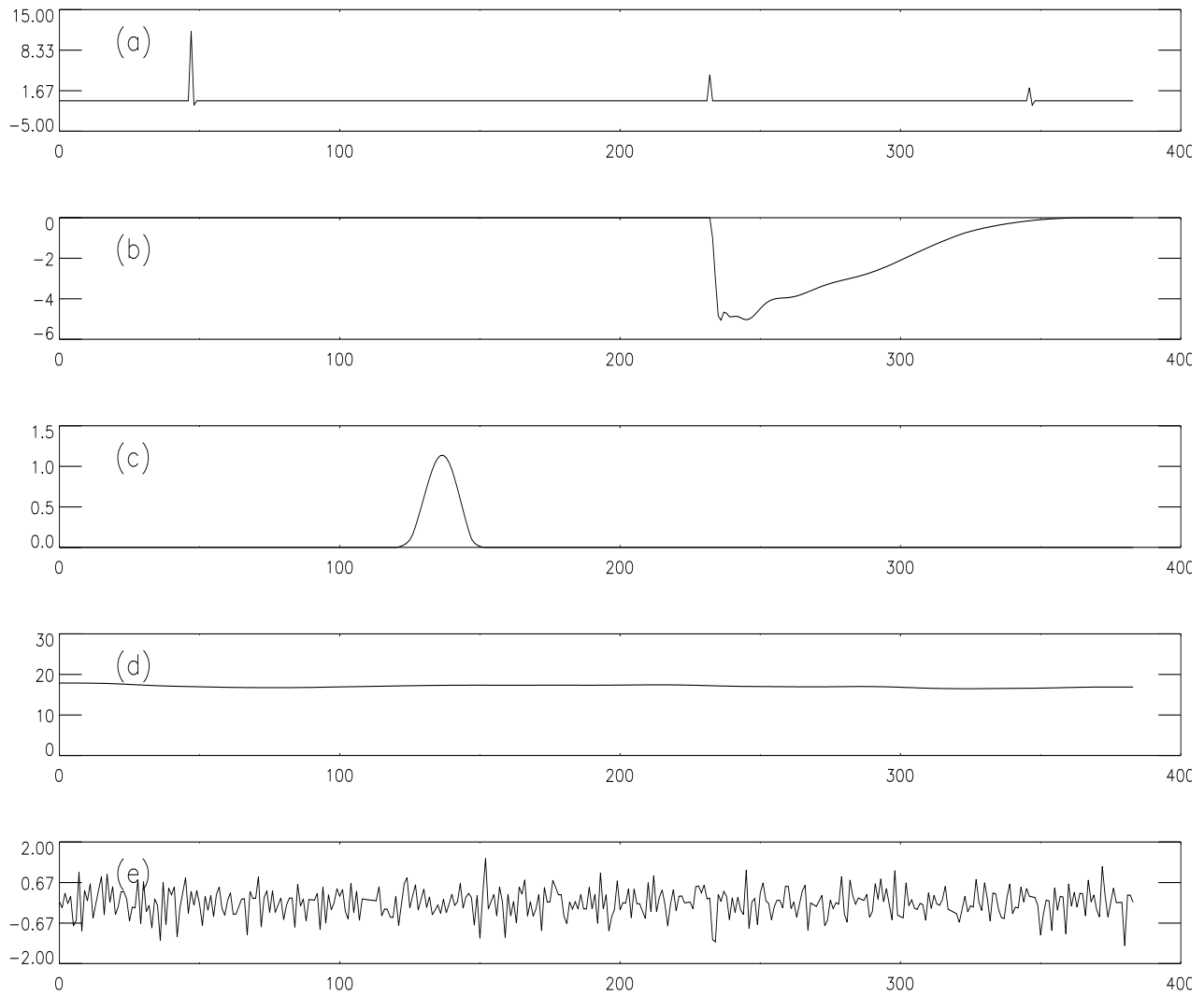
Figure 26: Decomposition of the signal into its principal components: (a) short glitch, (b) glitch negative tail, (c) source, (d) baseline, (e) noise. The simple sum of the five components is exactly equal to the original data (see Figure 2). The calibrated background-free data are obtained by addition of signals (c) and (e).
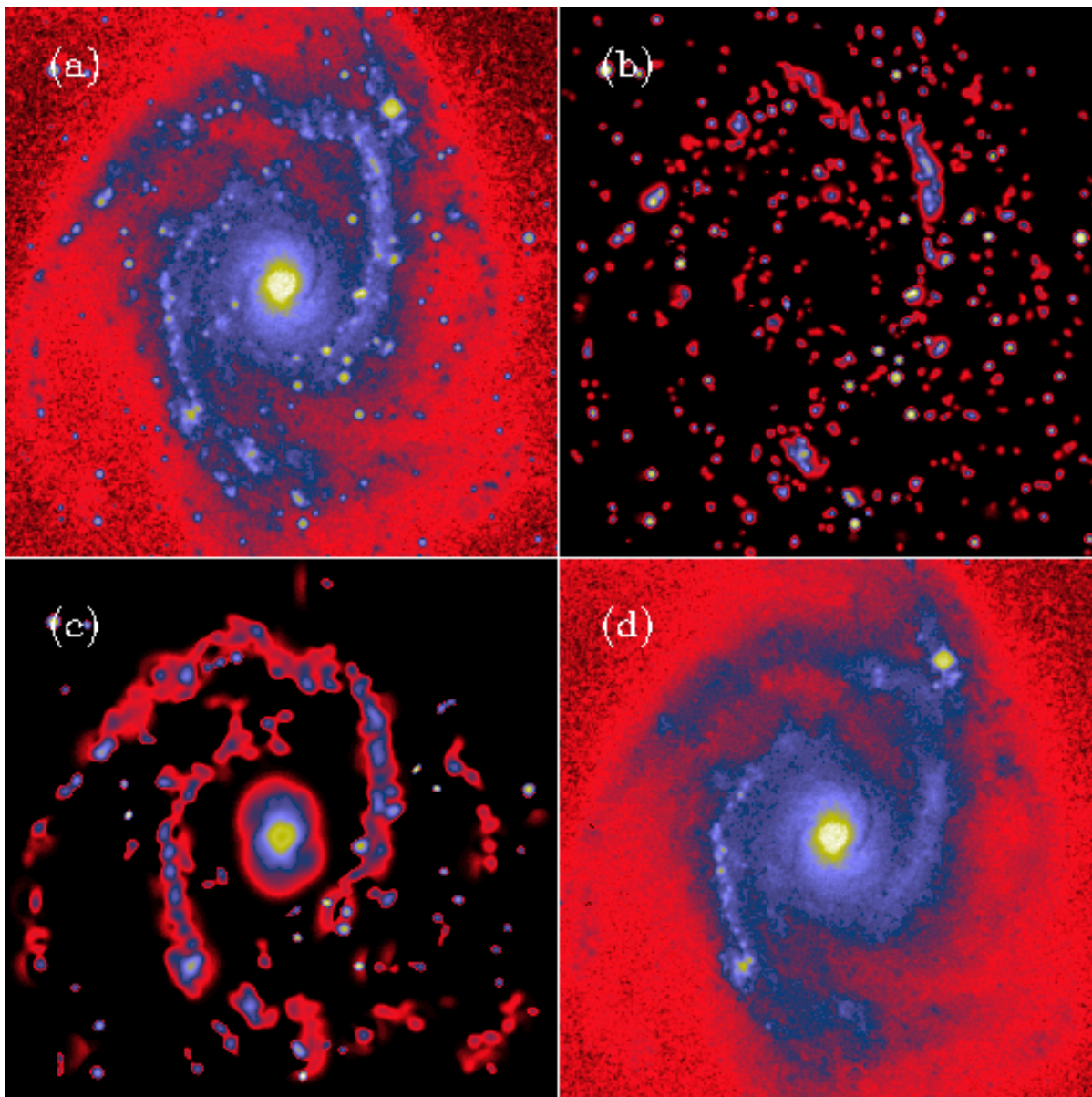
Figure 27: (a) Galaxy NGC2997, (b) objects detected from scale 1 to 2, (c) objects detected from scale 3 to 6, and (d) difference between (a) and (b).

References

[1] D. I. Barnea and H. F. Silverman. A Class of Algorithms for Fast Digital Image Registration. *IEEE Transactions on Computers.*, C-21(2):179–186, February 1972.

[2] A. Bijaoui and F. Rué. A multiscale vision model adapted to astronomical images. *Signal Processing*, 46:229–243, 1995.

[3] A. Bijaoui, J.L. Starck, and F. Murtagh. Restauration des images multi-echelles par l'algorithme à trous. *Traitement du Signal*, 3:11, 1994.

[4] Tj.R. Bontekoe, E. Koper, and D.J.M. Kester. Pyramid maximum entropy images of iras survey data. *AA*, 294:1037–1053, 1994.

[5] J.P. Burg. Annual Meeting International Society Exploratory Geophysics, Reprinted in Modern Spectral Analysis, 1978, D.G. Childers, ed., IEEE Press, New York, 34–41, 1978, 1967.

[6] C.J. Cesarsky, A. Abergel, P. Agnese, et al. Isocam in flight. *Astronomy and Astrophysics*, 315:L32, 1996.

[7] A. Claret, H. Dzitko, J. Engelmann, and J.-L. Starck. Glitch effects in isocam detectors. *Experimental Astronomy*, 1999. in press.

[8] J.P. Djamdji, A. Bijaoui, and R. Maniere. Geometrical registration of images: the multiresolution approach. *Photogrammetric Engineering and Remote Sensing.*, 59(5):645–653, May 1993.

[9] J.P. Djamdji, A. Bijaoui, and R. Maniere. Geometrical Registration of Remotely Sensed Images with the Use of the Wavelet Transform. *SPIE's International Symposium on Optical Engineering and Photonics*, pages 412–422, 12-16 April - Orlando 1993. Volume 1938.

[10] D.L. Donoho. Nonlinear wavelet methods for recovery of signals, densities, and spectra from indirect and noisy data. *Proceedings of Symposia in Applied Mathematics*, 47, 1993.

[11] B.R. Frieden. *Image Enhancement and Restoration*. Springer-Verlag, Berlin, 1978.

[12] S.F. Gull and J. Skilling. *MEMSYS5 Quantified Maximum Entropy User's Manual*, 1991.

[13] L. Huang and A. Bijaoui. Astronomical image data compression by morphological skeleton transformation. *Experimental Astronomy*, 1:311–327, 1991.

[14] R. Jeansoulin. *Les images multi-sources en télédétection: Mise en correspondance numérique et analyse de la structure géométrique*. PhD thesis, Université Paul Sabatier de Toulouse, 15 Juin 1982.

[15] M. Louys, J.-L. Starck, S. Mei, F. Bonnarel, and F. Murtagh. Astronomical image compression. *Astronomy and Astrophysics, Suppl. Ser.*, 136:579–590, 1999.

[16] F. Murtagh and J.L. Starck. Pattern clustering based on noise modeling in wavelet space. *Pattern Recognition*, 31(7):847–855, 1998.

[17] F. Murtagh and J.L. Starck. Overcoming the curse of dimensionality in clustering by means of the wavelet transform. *IEEE Expert*, 1999. in press.

[18] F. Murtagh, J.L. Starck, and A. Bijaoui. Image restoration with noise suppression using a multiresolution support. *Astronomy and Astrophysics, Suppl. Ser.*, 112:179–189, 1995.

[19] F. Murtagh, J.L. Starck, and A. Bijaoui. Multiresolution in astronomical image processing: A general framework. *The International Journal of Image Systems and Technology*, 6:332–338, 1995.

[20] F. Murtagh, J.L. Starck, and M. Louys. Very high quality image compression based on noise modeling. *International Journal of Imaging Systems and Technology*, 9:38–45, 1998.

[21] R. Narayan and R. Nityananda. Maximum entropy image restoration in astronomy. *Ann. Rev. Astron. Astrophys.*, 24:127–170, 1986.

[22] E. Pantin and J.L. Starck. Deconvolution of astronomical images using the multiscale maximum entropy method. *Astronomy and Astrophysics, Suppl. Ser.*, 315:575–585, 1996.

[23] M. Pierre and J.L. Starck. X-ray structures in galaxy cores. *Astronomy and Astrophysics*, 128(3):801–818, 1998.

[24] W.K. Pratt. *Digital Image Processing*. John Wiley & Sons, a wiley-interscience publication edition, 1991.

[25] R. Siebenmorgen, J.L. Starck, D.A. Cesarsky, S. Guest, and M. Sauvage. Isocam data users manual version 2.1. Technical Report SAI/95-222/Dc, ESA, 1996.

[26] J.L. Starck, A. Abergel, H. Aussel, M. Sauvage, R. Gastaud, A. Claret, X. Desert, C. Delattre, and E. Pantin. Isocam data processing. *Astronomy and Astrophysics, Suppl. Ser.*, 134:135–148, 1999.

[27] J.L. Starck, H. Aussel, D. Elbaz, and C. Cesarsky. Faint source detection with isocam using the preti method. In G.A. Mamon, Trinh Xuân Thuân, and J. Trân Thanh Vân, editors, *Extragalactic Astronomy in the Infrared*, pages 481–486. Editions Frontières, 1997.

[28] J.L. Starck, H. Aussel, D. Elbaz, D. Fadda, and C. Cesarsky. Faint source detection in isocam images. *Astronomy and Astrophysics*, 1999. submitted.

[29] J.L. Starck, A. Bijaoui, B. Lopez, and C. Perrier. Image reconstruction by the wavelet transform applied to aperture synthesis. *Astronomy and Astrophysics*, 283:349–360, 1994.

[30] J.L. Starck, A. Bijaoui, and F. Murtagh. Multiresolution support applied to image filtering and deconvolution. *CVGIP: Graphical Models and Image Processing*, 57:420–431, 1995.

[31] J.L. Starck and F. Murtagh. Image restoration with noise suppression using the wavelet transform. *Astronomy and Astrophysics*, 288:343–348, 1994.

[32] J.L. Starck and F. Murtagh. Automatic noise estimation from the multiresolution support. *Publications of the Astronomical Society of the Pacific*, 110(744):193–199, 1998.

[33] J.L. Starck and F. Murtagh. Multiscale entropy filtering. *Signal Processing*, 1999. in press.

[34] J.L. Starck, F. Murtagh, and A. Bijaoui. *Image Processing and Data Analysis: The Multiscale Approach*. Cambridge University Press, Cambridge (GB), 1998.

[35] J.L. Starck, F. Murtagh, and R. Gastaud. A new entropy measure based on the wavelet transform and noise modeling. Special Issue on Multirate Systems, Filter Banks, Wavelets, and Applications of *IEEE Transactions on CAS II*, 45(8), 1998.

[36] J.L. Starck, F. Murtagh, B. Pirenne, and M. Albrecht. Astronomical image compression based on noise suppression. *Publications of the Astronomical Society of the Pacific*, 108:446–455, 1996.

[37] J.L. Starck and M. Pierre. Structure detection in low intensity x-ray images. *Astronomy and Astrophysics, Suppl. Ser.*, 128, 1998.

[38] J.L. Starck, R. Siebenmorgen, and R. Gredel. Spectral analysis by the wavelet transform. *Astrophysical Journal*, 482:1011–1020, 1997.

[39] N. Weir. Application of maximum entropy techniques to hst data. In *3rd ESO/ST-ECF Data Analysis Workshop*, 1991.

[40] N. Weir. A multi-channel method of maximum entropy image restoration. In D.M. Worral, C. Biemesderfer, and J. Barnes, editors, *Astronomical Data Analysis Software and System 1*, pages 186–190. Astronomical Society of the Pacific, 1992.